THE JOURNAL OF PHYSICAL CHEMISTRY A

pubs.acs.org/JPCA Article

# Seed–Adsorbate Interactions as the Key of Heterogeneous Butanol and Diethylene Glycol Nucleation on Ammonium Bisulfate and Tetramethylammonium Bromide

Fatemeh Keshavarz,* Theo Kurtén, Hanna Vehkamäki, and Juha Kangasluoma

Cite This: J. Phys. Chem. A 2020, 124, 10527–10539 Read Online

ACCESS | Metrics & More | Article Recommendations | Supporting Information

**ABSTRACT:** Condensation particle counter (CPC) instruments are commonly used to detect atmospheric nanoparticles. They operate on the basis of condensing an organic working fluid on the nanoparticle seeds to grow the particles to a detectable size, and at the size of few nanometers, their efficiency depends on how well the working fluid interacts with the seeds under the measurement conditions. This study models the first steps of heterogeneous nucleation of two working fluids commonly used in CPCs (diethylene glycol (DEG) and *n*-butanol) onto two positively charged seeds, ammonium bisulfate and tetramethylammonium bromide. The nucleation process is modeled on a molecular level using a combination of systematic configurational sampling and density functional theory (DFT). We take into account the conformational flexibility of DEG and *n*-butanol and determine the key factors that can improve the efficiency of nanoparticle measurements by CPCs. The results show that hydrogen bonding between the seed and the working fluid molecules is central to the adsorption of the first DEG/*n*-butanol molecules onto the seeds. However, intermolecular hydrogen bonding between the adsorbed molecules can also enhance the nucleation process for the weakly adsorbing vapor molecules. Accordingly, the heterogeneous nucleation probability is higher for working fluid–nanoparticle combinations with a higher potential for hydrogen bonding; in this case, DEG and ammonium bisulfate. Moreover, conformational analysis and methodology evaluations indicate that the consideration of adsorbate conformers and step-wise addition of the vapor molecules to the seeds is not essential for qualitative modeling of heterogeneous nucleation systems, at least for systems where the adsorbate and seed chemical properties are clearly different. This is the first molecular-level modeling study reporting detailed chemical reasons for experimentally observed seed and working fluid preferences in CPCs and reproducing the experimental observations. Our presented approach can be likely used for predicting preferences in similar nucleating systems.

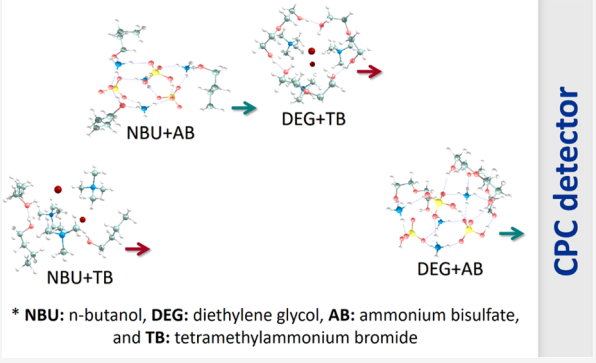




## 1. INTRODUCTION

Airborne ultrafine particles (UFPs, diameter <100 nm) exist in many atmospheric and industrial environments[1−3] and play an important role in, for example, cloud condensation nuclei formation and air pollution,[4,5] affecting cloud properties and human health.[6,7] A large fraction of the atmospheric UFPs originates from secondary pathways of clustering and condensation of vapors.[8] Therefore, the dynamics of such molecular processes should be accurately quantified, starting from small-sized clusters to understand and control UFP formation.

Nearly all experimental methods widely used to detect the dynamics of sub-10 nm nanoparticles rely on heterogeneous nucleation, a process in which a vapor condenses onto seed particles.[9] Condensation particle counters (CPCs) based on this process typically operate so that the flow containing the particles of interest is saturated with vapor at high temperatures and is subsequently cooled down to create vapor supersaturation.[10,11] In the supersaturated cold section of the instrument, heterogeneous nucleation and vapor condensation take place and the particles are grown to optical sizes for laser-based detection. The most common condensable vapors used in CPCs are butanol, water, and diethylene glycol (DEG), for which various reactor geometries have been designed.

The general characteristic of a CPC is its detection efficiency curve: heterogeneous nucleation probability of the sample particles as a function of particle size. Typically, the most important parameter considered to determine heterogeneous nucleation probability is the particle size (lower nucleation probability for smaller particles), while several studies have demonstrated that chemical interactions between the particles and the condensing vapor strongly affect the nucleation

Received: September 14, 2020
Revised: November 11, 2020
Published: December 3, 2020





https://dx.doi.org/10.1021/acs.jpca.0c08373
J. Phys. Chem. A 2020, 124, 10527−10539

probability at constant particle size.[12−16] Uncertainty in the detection efficiency curve results in uncertainty in the measured nanoparticle concentrations, especially in systems where secondary particle formation takes place, and this deteriorates the accuracy of the inferred aerosol dynamics.

Of specific interest, especially in the field of atmospheric sciences, is vapor condensation onto hydrocarbon seeds, as experiments have demonstrated that heterogeneous nucleation onto any substance other than hydrocarbons is more favorable.[14,16,17] Unfortunately, atmospherically relevant hydrocarbon production methods have been mostly used only in single laboratory experiments, and CPCs are typically calibrated using metal particles or salts, but a significant fraction of atmospheric nanoparticles in the boundary layer (particularly in forest environments) are expected to be mainly composed of oxidized hydrocarbons.[18] Therefore, accurate particle concentration measurement in environments where the particle composition is expected to be hydrocarbon dominated (especially in the sub-5 nm size range) remains a challenge.[9] Before attempting to model heterogeneous nucleation on top of poorly characterized and complex hydrocarbon surfaces, we need to investigate if our modeling methods are capable of reproducing experimental trends for the well-characterized seeds for which accurate data are available. Experimental studies have reported a larger heterogeneous nucleation probability of ammonium sulfate clusters compared to alkyl halide clusters at constant electrical mobility either with DEG or butanol as the condensing vapor.[14,19,20] On the other hand, DEG has been shown to be able to grow ions at 1 nm (mobility diameter) even at close to unity efficiency,[13,21] while high-efficiency detection with butanol is typically limited to somewhere around 2 nm.[16]

Molecular-level modeling approaches have been used to study atmospheric clustering but have not been applied directly to processes relevant in the current CPCs. Oh et al.[22] showed negative charge preference in water nucleation using small-ensemble umbrella sampling Monte Carlo (MC) simulation, and Nadykto et al.[23] demonstrated negative charge preference in binary water−sulfuric acid nucleation by applying quantum chemical modeling (density functional theory (DFT) calculation at the PW91PW91/6-311++G(3df,3pd) level). Kurtén et al.[24] studied the binding preferences of sulfuric acid to other atmospherically relevant molecules through DFT and ab initio quantum chemical calculations at the RI-MP2/aug-cc-pV(T+d)Z//BLYP/DZP and MP2(full)/6-311++G(3df,3pd) levels of theory. Zhang et al.[25] observed enhanced sulfuric acid−ammonia nucleation in the presence of glycolic acid by adopting a combination of DFT calculations at the M06-2X/6-311++G(3df,3pd) level and Atmospheric Clusters Dynamic Code (ACDC) for cluster distribution modeling. Wang et al.[26] reported improved sulfuric acid−water nucleation in the presence of formaldehyde through cluster sampling by the Basin-Hopping structure search algorithm, DFT studies at the PW91PW91/6-311++G(3df,3pd) level, and modeling by ACDC. The quantum chemical modeling methods used in these studies are applicable to the first steps of heterogeneous nucleation as well, which is the purpose of this study in the context of particle detection in CPCs.

We investigate the first steps of condensation of two condensable vapors commonly used in CPC-based measurements (*n*-butanol and DEG) onto positively charged ammonium bisulfate and tetramethylammonium bromide clusters of approximately the same volume. The aim is to understand in detail why the ammonium bisulfate clusters are more effective seeds than tetramethylammonium bromide clusters when using both DEG and *n*-butanol as the condensing fluid and also why DEG condenses more effectively on both of these seeds compared to *n*-butanol.

## 2. COMPUTATIONAL DETAILS

To model the starting steps of the heterogeneous nucleation process, an affordable but reliable computational level, representative seed models, different conformers of the DEG and *n*-butanol compounds, and an efficient nucleation simulation method were required. For the selection of the computational level, we compared different computational methods, which had all been previously used to model either ammonium bisulfate or tetramethylammonium bromide clusters or ion pairs. The most commonly used ab initio and density functional theory (DFT) methods in such studies include B3LYP,[27−32] CAM-B3LYP,[33] M06-2X,[28,34] MP2,[27,28,32,35−37] PW91PW91[38,39] (or PW91[27,28,34]), and ωB97X-D.[40] In the literature, these methods have been used along with various basis sets. Here, the def2-TZVP[41,42] basis set was applied as the main basis set to all methods because of its low computational cost and high accuracy.[43] The choice of the computational level was justified by evaluating the outlined methods and several additional basis sets against experimental data or CCSD(T) calculations on the ion-pair binding energy and the geometry (structure) of the involved molecules or clusters. Throughout this study, all DFT and MP2 calculations were carried out using Gaussian 16, Revision A.03,[44] while the DLPNO-CCSD(T) energies were computed using Orca 4.1.1.[45] Figure S1 and Table S1, respectively, compare the geometry of the optimized molecules and the calculated ion-pair binding energies with the experimental data or the CCSD(T) results reported using the largest basis set. As can be seen from Figure S1, all tested computational levels can predict the free molecular geometries with high precision. However, Table S1 suggests that MP2/def2-TZVP is the most accurate level of theory for the prediction of ion-pair binding energies. Since MP2 calculations are too demanding for the largest clusters studied here, the next best method, i.e., ωB97X-D/def2-TZVP, was chosen as the final computational level. It should be noted that ωB97X-D has been previously identified as an efficient and highly accurate hybrid functional for the prediction of thermochemical and molecular properties[46] as it can treat both dispersion (long-range electron correlation) and electrostatic interactions appropriately.[47] Nevertheless, while DFT methods such as ωB97X-D may not be accurate enough for a quantitative treatment of clustering and chemical reactions, some studies employing a combination of DFT calculations, coupled cluster energy corrections, detailed balance, and kinetic gas theory collision rates[48] for modeling of homogeneous nucleation have shown that DFT-based calculations can nevertheless result in good agreement with experimental particle formation rates. This implies that DFT-based cluster energetics can be sufficiently reliable, especially for qualitative insight into differences between chemical systems. We note that the clustering "barriers" discussed here are thermodynamic rather than kinetic, as no covalent bonds break or form during the clustering processes studied here, and they are unlikely to be associated with transition states in the sense of chemical kinetics.

To simulate the experimental nucleation process, positively charged seeds with approximately equal volumes were compared. To generate seed (cluster) structures from the constituent ions, a systematic configurational sampling


https://dx.doi.org/10.1021/acs.jpca.0c08373
J. Phys. Chem. A 2020, 124, 10527−10539

method[49] was followed. In this approach, the construction and optimization of the seed clusters were broken into four steps. In step one, the artificial bee colony (ABC) algorithm implemented in the ABCluster 1.4 program[50,51] was employed to generate 500 local minima (LM) structures for each seed type. The ABC algorithm was first used to guess 700 starting configurations. Next, 4 scout bees were evoked to search the created population space in pursuit of the most stable LM structures. In each cycle, the scout bees continued searching and regenerating configurations 200 times. The energy of each generated structure was computed as the sum of Lennard-Jones (LJ) and Coulombic energy terms. The Coulombic interactions were computed based on the charges retrieved from atomic polar tensor (APT) calculations at the ωB97X-D/def2-TZVP level using the optimized cluster constituents. The LJ parameters were adopted from different sources, i.e., the studies of Olsen et al.[52] (for DEG) and Cerar et al.[53] (CHARMM, for *n*-butanol), and Dreiding force field[54] (for bromide, tetramethylammonium,[55] ammonium, and bisulfate). At this stage, the molecules were kept rigid (i.e., all intramolecular bond lengths, angles, and dihedrals were all kept fixed). Of all generated molecular configurations, the 500 structures with the lowest energy values were passed to the second step. In this step, these 500 geometries were optimized using the low-cost, fast, and robust GFN-xTB[56] semiempirical method as implemented in the XTB 6.0.1 program.[57] An energy cut-off of 100 kJ $mol^{-1}$ was employed, structurally highly similar configurations were filtered out, and a maximum of 35 structures were passed on from this step to the third step. In the third step, the remaining structures were reoptimized at the ωB97X-D/6-31+G* level. In this step, the harmonic frequencies of all structures were also computed to verify the local minima nature of the structures. In the last configurational sampling step, seven of the reoptimized geometries with the lowest Gibbs free energies ($G$) were selected and reoptimized at the ωB97X-D/def2-TZVP level. Among the seven geometries, the structure giving the lowest $G$ value was finally accepted as a representative seed structure for the actual clustering simulations. The lowest energy $(NH_4^+)_4(HSO_4^-)_3$ (shorthand notation for this cluster is **A4B3**; volume is 233.261 $cm^3$ $mol^{-1}$) and $((CH_3)_4N^+)_3(Br^-)_2$ (shorthand notation for this cluster is **T3B2**; volume is 292.943 $cm^3$ $mol^{-1}$) geometries were chosen as representative seed structures. (The volumes were computed using a 0.001 electrons $Bohr^{-3}$ isosurface at the ωB97X-D/def2-TZVP level; the standard setting in the Gaussian 16 program.) The obtained A4B3 structure is compared with the previously reported A4B3 structures in Figure S2. The figure demonstrates that the applied configurational sampling method is successful in finding the global minimum structure of the seeds. All calculated and reported thermochemical values in this study refer to 298.15 K and 1 atm reference pressure.

We next generated a representative set of conformers for the DEG and *n*-butanol molecules. This is necessary since the lowest-energy conformer in the gas phase may not be the lowest-energy conformer when adsorbed at a seed surface. *n*-Butanol has 14 unique conformers, which have been presented and studied in detail by Black and Simmie[58] and Moc et al.[59] For DEG, to the best of our knowledge, no previous study has fully explored the conformational space, and most studies have been restricted to the lowest-energy conformer. Therefore, extensive dihedral scanning and frequency calculations were performed on the DEG structure reported by Olsen et al.[52] to find the various DEG conformers. Many of the identified conformers converged into their enantiomeric counterparts with identical energies. Therefore, only the conformers with distinctive $G$ values were used here (see Figure 1). After having the complete list of *n*-butanol and DEG conformers, 5 conformers of each organic compound were selected based on their energy and geometry diversity (including both the lowest- and highest-energy gas-phase conformer, and 3 additional conformers with as different structures and potential H-bonding patterns as possible), and the clustering simulations were performed using these conformers. The five selected *n*-butanol and DEG conformers are shown in Figure 1.

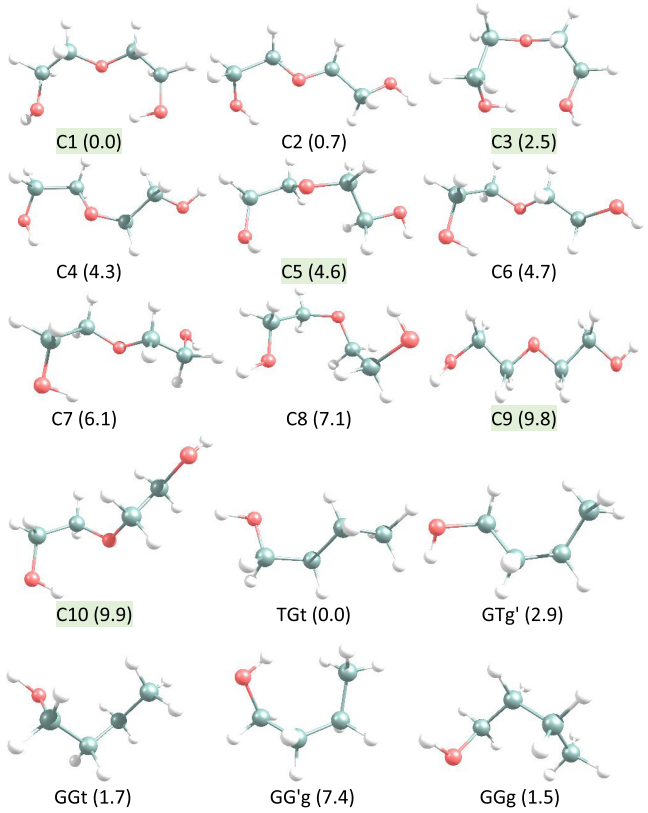


**Figure 1.** Geometries of the distinctive conformers of DEG (C1 to C10) and the selected five conformers of *n*-butanol (TGt, GTg′, GGt, GG′g, and GGg) optimized at the ωB97X-D/def2-TZVP level of theory. The values refer to the Gibbs free energy (kJ $mol^{-1}$) of the structures at 298.15 K and 1 atm relative to the lowest-energy geometry. The DEG structures selected for further studies are highlighted.

After preparing the required starting structures, the nucleation process was simulated by adding the DEG and *n*-butanol conformers to the seeds. Ten clusters containing one of the A4B3 or T3B2 seeds and one *n*-butanol or DEG conformer were generated using the configurational sampling method described above (application of the ABC algorithm, optimization of the generated LM geometries using GFN-xTB, filtering of results, reoptimizing the structures at the ωB97X-D/6-31+G* level, and refiltering and reoptimizing at the ωB97X-D/def2-TZVP level). The adsorbate−seed cluster with the lowest adsorption Gibbs free energy ($\Delta G$) was selected for the next step. Importantly, the adsorption $\Delta G$ values of all conformers were calculated with respect to the energy of the most stable (lowest energy) DEG and *n*-butanol conformers in the gas phase (i.e., C1 and TGt, respectively). Next, the four selected A4B3/DEG, A4B3/*n*-butanol, T3B2/DEG, and T3B2/*n*-butanol clusters were treated


https://dx.doi.org/10.1021/acs.jpca.0c08373
J. Phys. Chem. A 2020, 124, 10527−10539

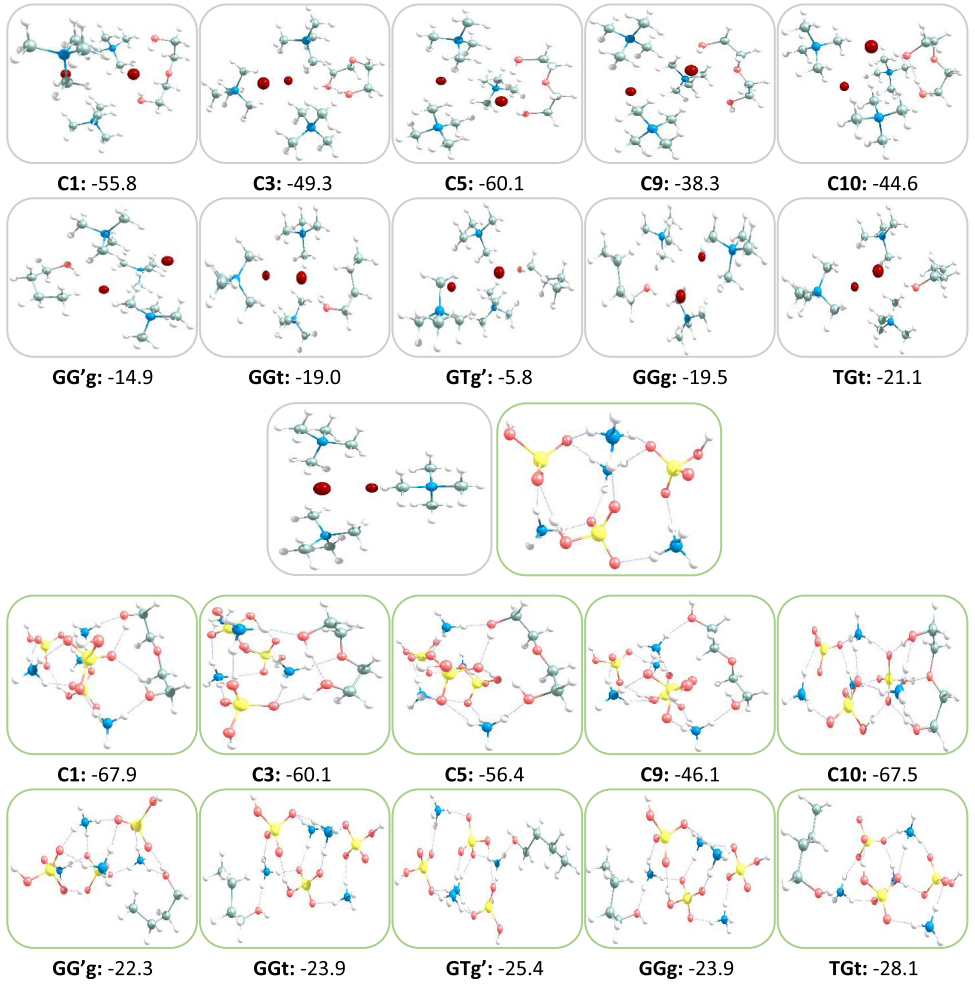


**Figure 2.** Adsorption mode of DEG and *n*-butanol on $((CH_3)_4N^+)(Br^-)_2$ (T3B2, the gray panels) and $(NH_4^+)_4(HSO_4^-)_3$ (A4B3, the green panels). The binding Gibbs free energy of the organic adsorbates are given in kJ mol$^{-1}$. The blue dotted lines represent strong hydrogen bonding.

as single molecules in the ABC configurational sampling with APT charges being recalculated for the clusters, and five DEG or *n*-butanol conformers were again separately added to them, generating 10 clusters for each system using the same configurational sampling approach. Again, the lowest free energy structure was selected for each (seed)(adsorbate)$_2$ system and passed to the next step, in which a third molecule was added in exactly the same way. In other words, at each stage, 20 separate sets of configurational sampling calculations were run to form 20 clusters, each containing one A4B3 or T3B2 seed and one to three molecules of DEG or *n*-butanol (with five conformations of each considered in each step). In parallel to this "step-wise" approach, we also separately investigated the clustering of the most stable *n*-butanol (TGt) and DEG (C1) conformers as well as the surprisingly weakly adsorbing *n*-butanol conformer (GTg′). These calculations were performed as described above, but just one conformer of *n*-butanol or DEG was used in each step. For the generation of the (seed)(adsorbate)$_2$ and (seed)(adsorbate)$_3$ clusters, we also studied the outcome of adding all adsorbate molecules to the seeds "simultaneously" (instead of adding one at a time as described above) through the described configurational sampling method. The purpose of these calculations was both to gain more understanding of the structural factors affecting the heterogeneous nucleation process and to evaluate the magnitude of the effect of conformer selection on the final results. Furthermore, natural bond-orbital analysis (NBO) was performed on the resultant seed−DEG/*n*-butanol clusters at the ωB97X-D/def2-TZVP level to gain insight into the seed−molecule interactions and understand the reasons behind the different performances of the two seeds. The NBO outputs were also analyzed to depict the charge transfer trends driven by the adsorption of DEG and *n*-butanol on the two seeds in the form of electrostatic potential (ESP) surfaces.

## 3. RESULTS AND DISCUSSION

The first process in the growth of nanoparticles (seeds) to detectable size is the adsorption of one single or several working fluid molecules onto the sample seeds. Figure 2 shows the free energies ($\Delta G$) for the adsorption of different *n*-butanol and DEG conformers onto the two studied seeds. For the DEG conformers, the values lie between −38.3 and −60.1 kJ mol$^{-1}$ on T3B2 and −46.1 and −67.9 kJ mol$^{-1}$ on A4B3, while for *n*-butanol the adsorption free energies range from −5.8 to −21.1 kJ mol$^{-1}$ for T3B2 and from −22.3 to −28.1 kJ mol$^{-1}$ for A4B3. Clearly, both seeds adsorb DEG more strongly compared with *n*-butanol. Also, it is evident that A4B3 outperforms T3B2 in the adsorption of both organic adsorbates. In other words, the lowest $\Delta G$ values (i.e., the strongest adsorption modes) are observed for the adsorption of DEG conformers on A4B3 and the highest $\Delta G$ results (i.e., the weakest adsorption modes) are


https://dx.doi.org/10.1021/acs.jpca.0c08373
J. Phys. Chem. A 2020, 124, 10527−10539

associated with the adsorption of the *n*-butanol conformers on the T3B2 seed.

These computational results cannot be directly compared to experimental observations, as CPCs measure the particles that have grown beyond the critical seed-working fluid cluster size, and the nucleation process is inherently dynamic. To simulate nucleation dynamics, we would first need to know the size and composition of the critical cluster (corresponding to the free-energy barrier for nucleation). However, the critical cluster size (and even the very existence of a nucleation barrier) is highly dependent on the conditions, most importantly, the supersaturation. At low supersaturations, nucleation is associated with a high barrier (and a large critical cluster), while at high enough supersaturations the barrier disappears (and the critical cluster then contains just one working fluid molecule). Performing dynamic simulations for all possible supersaturation conditions is computationally extremely demanding, as very large cluster sizes would need to be included. The exact supersaturations corresponding to CPC measurements are also difficult to quantify for many vapors (specially DEG), and the supersaturations can change inside the instrument, making a quantitative comparison impossible even if the simulations could be performed. In this study, we therefore focus on comparing the first steps of the heterogeneous nucleation process for the four studied systems, and we use equilibrium cluster properties to qualitatively compare the seed−vapor nucleation probabilities. Weak seed−vapor interactions (resulting in high free energies of clustering) lead to the evaporation of the vapor molecules before collision and adsorption of further vapor molecules, while the reverse is true for strong seed−vapor interactions. In addition, the formation free energy of the critical cluster depends on seed−vapor (and vapor−vapor) interactions, which are already present also in the smallest seed−vapor clusters, and reflected in their thermodynamic properties.

Our modeling results are thus in line with the experimental results mentioned in the introduction,[14,19,20] assuming that the heterogeneous nucleation of the $((CH_3)_4N^+)_3(Br^-)_2$ (i.e.,T3B2) clusters is similar to the nucleation of other alkyl halides with longer alkyl chains. Thus, the chemical preference of both butanol and DEG to ammonium bisulfate over alkyl halides is well supported by the experimental findings. An exact quantitative experimental comparison of DEG and *n*-butanol as working fluids is not straightforward as the inferred preferences are based on the heterogeneous nucleation probability that is dependent on the supersaturation inside the instrument. Retrospective analysis of the true supersaturation field inside the instruments is challenging, but we can make a comparison at least to one experimental study,[19] in which the supersaturation inside the instruments was fixed such that homogeneous nucleation was just barely starting to take place. This tuning was used to make the observed size-resolved heterogeneous nucleation probabilities comparable between different instruments operating with different working fluids. The computational results of this study indeed replicate the preferences observed in ref 19, in which DEG nucleation is more preferable than butanol for both ammonium bisulfate and alkyl halides, while also ammonium bisulfate nucleation is more preferable than alkyl halide nucleation with both DEG and butanol.

According to Figure 1, the two seeds also act differently toward the various conformers of *n*-butanol and DEG. For instance, A4B3 adsorbs C1 most strongly (C1: $\Delta G = -67.9$ kJ mol$^{-1}$ vs C9: $\Delta G = -46.1$ kJ mol$^{-1}$) while T3B2 can adsorb C5 the best (C5: $\Delta G = -60.1$ kJ mol$^{-1}$ vs C9: $\Delta G = -38.3$ kJ mol$^{-1}$). In general, both seeds show some level of selectivity during the adsorption of the DEG conformers, but they distinguish between the various *n*-butanol conformers to a less extent. The only exception to this is the adsorption of GTg′ on T3B2. Eventually, the $\Delta G$ values of GG′g, GGt, GGg, and TGt adsorption on T3B2 fall within the range of −14.9 to −21.1 kJ mol$^{-1}$, with TGt giving the best $\Delta G$ value (−21.1 kJ mol$^{-1}$). However, GTg′ adsorption on T3B2 gives a significantly different $\Delta G$ value (i.e., −5.8 kJ mol$^{-1}$) even though the $\Delta G$ value of this conformer is close to the $\Delta G$ results of the other conformers for A4B3. Therefore, the results displayed in Figure 1 raise several questions: Why do the seeds prefer adsorbing DEG? Why A4B3 outperforms T3B2? What makes GTg′ adsorb weakly on T3B2? To answer these questions, the geometries, thermodynamics of adsorption, and the underlying interactions were studied in detail.

A close look at Figure 2 shows that T3B2 conserves its structure upon adsorption of the DEG and *n*-butanol conformers. However, the constituents of the A4B3 seed rearrange slightly to enable stronger interaction with the adsorbates. Generalizing somewhat, it seems that T3B2 needs a balanced (symmetrical) distribution of its $(CH_3)_4N^+$ constituents around the axial $Br^-$ anions to retain its stability. In addition, the large size of the $(CH_3)_4N^+$ cations restricts the adsorption of the DEG and *n*-butanol adsorbates. On the other hand, the components of A4B3 can rearrange into various configurations (including different H-bonding patterns) while conserving their structural stability (see Figure S2 for examples of some stable A4B3 configurations). These structural differences may cause the difference in the adsorption performance of the two seeds.

We further analyzed the binding thermodynamics to separate entropic contributions (resulting from, e.g., structural flexibility) from enthalpic contributions related to the binding energies. Table 1 reports the zero-point energy corrected electronic energy ($\Delta E$), potential energy ($\Delta U$), enthalpy ($\Delta H$), and entropy ($\Delta S$) of DEG and *n*-butanol adsorption on the two seeds, in addition to the $\Delta G$ values outlined in Figure 2. As with all clustering or association processes, the adsorption of all conformers on both seeds is enthalpy driven, as the entropy changes are always negative due to the loss of rotational and translational degrees of freedom. Furthermore, the contribution of the $-T\Delta S$ term to $\Delta G$ ($\Delta G = \Delta H - T\Delta S$) only varies by a maximum of 6.6 kJ mol$^{-1}$ from one seed to another. Therefore, the structural properties of the seeds (like their ability of hydrogen bonding) and the relevant interaction types, which affect adsorption enthalpy, might be the key to the observed differences, but structural flexibility does not have a crucial effect.

Because experimental nucleation probabilities can in principle be biased by homogeneous nucleation of the condensing fluid, the obtained adsorption enthalpies were compared with the vaporization enthalpies $\Delta H_{vap}$ of DEG (55.1−59.8 kJ mol$^{-1}$ at 273−540 K) and *n*-butanol (20.8−51.6 kJ mol$^{-1}$ at 236−523 K).[60] As expected, the adsorption enthalpies were much lower than the condensation enthalpies (minus one time the vaporization enthalpy), demonstrating that the heterogeneous process is much more favorable. This is not surprising as CPCs would fail if homogeneous nucleation dominated heterogeneous nucleation. It should be added that at sufficiently high vapor concentrations (irrelevant to CPC operating conditions), homogeneous nucleation would dominate over heterogeneous nucleation.



https://dx.doi.org/10.1021/acs.jpca.0c08373
J. Phys. Chem. A 2020, 124, 10527−10539

**Table 1. Thermodynamics of One DEG (Conformers C1, C3, C5, C9, and C10) or *n*-Butanol (Conformers GG′g, GGt, GTg′, GGg, and TGt) Molecule Adsorption on the $(NH_4^+)_4(HSO_4^-)_3$ (i.e., A4B3) and $((CH_3)_4N^+)_3(Br^-)_2$ (i.e., T3B2) Seeds, at the ωB97X-D/def2-TZVP Level[a]**

| adsorbate | ΔE | ΔU | ΔH | ΔG | ΔS |
|---|---|---|---|---|---|
| | | | $((CH_3)_4N^+)_3(Br^-)_2$ | | |
| C1 | −114.9 | −112.9 | −115.4 | −55.8 | −199.8 |
| C3 | −109.3 | −108.2 | −110.6 | −49.3 | −205.8 |
| C5 | −118.7 | −117.2 | −119.6 | −60.1 | −199.6 |
| C9 | −93.7 | −90.7 | −93.2 | −38.3 | −184.0 |
| C10 | −102.6 | −101.9 | −104.3 | −44.6 | −200.4 |
| GG′g | −59.1 | −54.9 | −57.4 | −14.9 | −142.6 |
| GGt | −70.5 | −67.4 | −69.9 | −19.0 | −170.6 |
| GTg′ | −51.8 | −47.6 | −50.0 | −5.8 | −148.5 |
| GGg | −69.0 | −65.7 | −68.2 | −19.5 | −163.1 |
| TGt | −68.1 | −63.9 | −66.4 | −21.1 | −152.0 |
| | | | $(NH_4^+)_4(HSO_4^-)_3$ | | |
| C1 | −120.0 | −118.5 | −120.9 | −67.9 | −178.0 |
| C3 | −118.9 | −119.6 | −122.1 | −60.1 | −207.8 |
| C5 | −120.1 | −119.4 | −121.9 | −56.4 | −219.8 |
| C9 | −102.4 | −100.8 | −103.3 | −46.1 | −191.8 |
| C10 | −128.8 | −129.8 | −132.3 | −67.5 | −217.1 |
| GG′g | −66.8 | −63.3 | −65.8 | −22.3 | −145.7 |
| GGt | −72.9 | −69.9 | −72.4 | −23.9 | −162.8 |
| GTg′ | −64.7 | −60.6 | −63.1 | −25.4 | −126.2 |
| GGg | −72.9 | −69.9 | −72.4 | −23.9 | −162.8 |
| TGt | −75.7 | −72.8 | −75.3 | −28.1 | −158.3 |

[a]ΔE, ΔU, ΔH, and ΔG are in kJ mol$^{-1}$, while ΔS is in J mol$^{-1}$. All data refer to 298.15 K and 1 atm.

*n*-Butanol is inherently more volatile than DEG (as reflected by the difference in vaporization enthalpies), and DEG condensation is thus more favorable if the vapor concentrations were equal. However, the preference of the studied seeds for DEG heterogeneous nucleation over *n*-butanol heterogeneous nucleation follows primarily from stronger seed−DEG interactions rather than from stronger self-clustering by DEG. This is demonstrated by the fact that the difference between the DEG adsorption $\Delta H$ values and the DEG $-\Delta H_{vap}$ is much larger than the corresponding difference for *n*-butanol.

NBO analysis was performed on the seed−adsorbate clusters giving the best ΔG values (i.e., A4B3/C1, T3B2/C5, A4B3/TGt, and T3B2/TGt), in addition to the T3B2/C1 cluster and clusters, including the GTg′ conformer, which gives an exceptionally high ΔG value for adsorption on T3B2. According to the NBO results (Tables 2 and S2), the interaction of DEG and *n*-butanol with both seeds is mainly driven by strong hydrogen bonding. The hydrogen-bonding interactions are associated with charge transfer from the lone-pair (LP) orbital of the hydrogen-bonding donors (such as the oxygen atom of $HSO_4^-$, any of the DEG/*n*-butanol oxygen atoms, or the $Br^-$ anions) to the antibonding σ-type (σ*) orbital of the hydrogen-bonding acceptors (like the OH moiety of DEG, *n*-butanol or $HSO_4^-$, the NH moiety in $NH_4^+$, and CH in $(CH_3)_4N^+$). In general, the higher the charge transfer between the hydrogen bond donors and acceptors, the higher the strength of the resultant hydrogen bonds. In T3B2, the best hydrogen-bonding donor is $Br^-$. Consequently, substantial charge transfer occurs from the LP orbitals of the $Br^-$ anions to the σ*(OH) orbitals of *n*-butanol and DEG. In the A4B3/DEG or *n*-butanol cluster, the most efficient hydrogen-bonding donor is the $LP(O_{OH})$ orbital of DEG or *n*-butanol, which transfers substantial charge to the σ*(NH) of the ammonium cations. Nevertheless, other types of charge transfer, mainly dispersion interactions, also help the adsorption process. However, their contribution is not as significant as hydrogen-bonding-related charge transfer. The most noticeable nonhydrogen bonding interactions refer to the

**Table 2. Second-Order Perturbation Energies ($E^{(2)}$ Stabilization Energy; kJ mol$^{-1}$) Associated with Charge Transfer from (Donor)/to (Acceptor) NBOs of DEG (Conformers C1 and C5) and *n*-Butanol (TGt Conformer) Adsorbed on the $(NH_4^+)_4(HSO_4^-)_3$ (i.e., A4B3) and $((CH_3)_4N^+)_3(Br^-)_2$ (i.e., T3B2) Seeds in the Form of NBO Type(atom/bond$_{unit}$)$_{seed\ or\ adsorbate}$[a]**

| $(NH_4^+)_4(HSO_4^-)_3$ | | | $((CH_3)_4N^+)_3(Br^-)_2$ | | |
|---|---|---|---|---|---|
| from | to | $E^{(2)}$ | from | to | $E^{(2)}$ |
| | C1 | | | C5 | |
| $LP(O_{HSO_4})_{seed}$ | $\sigma^*(OH_{OH\text{-}1})_{C1}$ | 10.2 | $LP(Br_{Br})_{seed}$ | $\sigma^*(OH_{OH\text{-}2})_{C5}$ | 5.3 |
| $LP(O_{HSO_4})_{seed}$ | $\sigma^*(OH_{OH\text{-}2})_{C1}$ | 12.6 | $LP(Br_{Br})_{seed}$ | $\sigma^*(OH_{OH\text{-}1})_{C5}$ | 53.1 |
| $LP(O_{HSO_4})_{seed}$ | $\sigma^*(OH_{OH\text{-}1})_{C1}$ | 8.5 | $LP(Br_{Br})_{seed}$ | $\sigma^*(OH_{OH\text{-}1})_{C5}$ | 6.9 |
| $LP(O_{HSO_4})_{seed}$ | $\sigma^*(OH_{OH\text{-}2})_{C1}$ | 14.1 | $LP(Br_{Br})_{seed}$ | $\sigma^*(OH_{OH\text{-}2})_{C5}$ | 71.6 |
| $\sigma^*(SO_{HSO_4})_{seed}$ | $\sigma^*(OH_{OH\text{-}1})_{C1}$ | 4.4 | $LP(O_{OH\text{-}1})_{C5}$ | $\sigma^*(CH_{TMA})_{seed}$ | 8.2 |
| $\sigma^*(SO_{HSO_4})_{seed}$ | $\sigma^*(OH_{OH\text{-}2})_{C1}$ | 4.5 | $LP(O_{OH\text{-}1})_{C5}$ | $\sigma^*(CH_{TMA})_{seed}$ | 6.6 |
| $LP(O_{OH\text{-}2})_{C1}$ | $\sigma^*(NH_{NH_4})_{seed}$ | 9.1 | $LP(O_{OH\text{-}2})_{C5}$ | $\sigma^*(CH_{TMA})_{seed}$ | 12.9 |
| $LP(O_{OH\text{-}2})_{C1}$ | $\sigma^*(NH_{NH_4})_{seed}$ | 115.3 | | | |
| $LP(O_{OH\text{-}1})_{C1}$ | $\sigma^*(NH_{NH_4})_{seed}$ | 10.7 | | | |
| $LP(O_{OH\text{-}1})_{C1}$ | $\sigma^*(NH_{NH_4})_{seed}$ | 97.5 | | | |
| | TGt | | | TGt | |
| $LP(O_{HSO_4})_{seed}$ | $\sigma^*(OH_{OH})_{TGt}$ | 6.2 | $LP(Br_{Br})_{seed}$ | $\sigma^*(OH_{OH})_{TGt}$ | 74.3 |
| $LP(O_{OH})_{TGt}$ | $\sigma^*(NH_{NH_4})_{seed}$ | 8.6 | $LP(O_{OH})_{TGt}$ | $\sigma^*(CH_{TMA})_{seed}$ | 12.6 |
| $LP(O_{OH})_{TGt}$ | $\sigma^*(NH_{NH_4})_{seed}$ | 133.9 | $LP(O_{OH})_{TGt}$ | $\sigma^*(CH_{TMA})_{seed}$ | 4.3 |

[a]The energy threshold of 4.2 kJ mol$^{-1}$ (=1 kcal mol$^{-1}$) is considered. In DEG, the hydroxyl and ether O atoms are respectively distinguished as $O_{OH\text{-}1}$ (and $O_{OH\text{-}2}$) and $O_c$. TMA represents $(CH_3)_4N^+$. Note that similar units in the seeds are not distinguished.



https://dx.doi.org/10.1021/acs.jpca.0c08373
J. Phys. Chem. A 2020, 124, 10527−10539

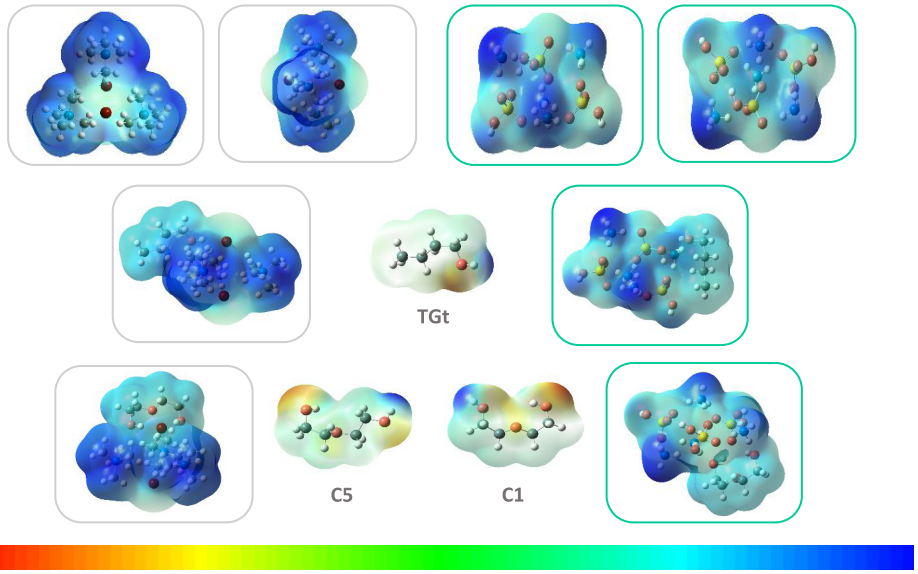


**Figure 3.** Changes in the charge density of the *n*-butanol and DEG adsorbates (conformers TGt, C1, and C5) upon adsorption on the $((CH_3)_4N^+)_3(Br^-)_2$ (i.e., T3B2, the gray panels) and $(NH_4^+)_4(HSO_4^-)_3$ (A4B3, the green panels) seeds, based on ESP analysis. The most positive and negative parts are, respectively, shown using the blue and red colors.

charge transfer from the $\sigma^*$(SO) orbitals of $HSO_4^-$ in A4B3 to the $\sigma^*$(OH) orbitals of C1.

Another fact highlighted in Tables 2 and S2 is that the $\Delta G$ values are directly correlated with the extent of charge transfer associated with hydrogen bonding. The sum of the $E^{(2)}$ stabilization energies, and even the number of significant charge transfer arrays, are higher for A4B3 (relative to T3B2) and DEG (relative to *n*-butanol). To be more specific, both DEG (with 3 oxygen atoms) and A4B3 (with multiple oxygen and nitrogen atoms and numerous N−H and O−H bonds) have a higher number of hydrogen-bonding donor and acceptor orbitals. That is why the seeds prefer adsorbing DEG, and A4B3 outperforms T3B2. One question still remains: What makes the GTg′ conformer adsorb so weakly on T3B2? Based on Figure 2, the *n*-butanol conformers require maximal contact with the $Br^-$ and $(CH_3)_4N^+$ ions for effective adsorption. However, the specific conformer of GTg′ forces its alkyl tail outwards from the seed. As an outcome, the strength of charge transfer from T3B2 to GTg′ is reduced, and GTg′ fails in transferring any significant amount of charge to the T3B2 seed (see Table S2). The case of T3B2/GTg′ and, in general, the NBO results, clearly suggest that for any organic compound, both a high potential for hydrogen bond formation and high conformational flexibility for maximizing the opportunity of hydrogen bond networking will assist the growth (and instrumental detection when used as a working fluid) of inorganic clusters, particularly clusters that are stabilized through hydrogen bonding.

Furthermore, the NBO results were visualized as ESP surfaces in Figure 3. As displayed in this figure, the adsorption of DEG and *n*-butanol causes some charge transfer trends that cannot be isolated from each other. In general, the seeds transfer some positive charge to the DEG and *n*-butanol molecules. Simultaneously, the DEG and *n*-butanol adsorbates transfer their negative charge accumulated on their hydroxyl and central oxygen groups to the seeds. The transferred charges redistribute among the seed components and the adsorbate moieties. In the end, the adsorbed DEG and *n*-butanol molecules obtain some net positive charge, and the $N(CH_3)_4^+$ ions share their positive charge with the adsorbates and the $Br^-$ anions partially, the $Br^-$ axis carries lower electron density, the $NH_4^+$ cations (especially those located near the adsorption site) lose their positive charge density significantly and the relatively positive charge of the O−H bonds in the $HSO_4^-$ components adjacent to the adsorbates redistribute to stabilize the adsorbates.

While single-molecule adsorption studies already reveal many of the key structural features behind heterogeneous nucleation, we next investigated whether the observed trends also hold for the adsorption of multiple molecules (allowing for inter-adsorbate interactions). To answer this question, two additional DEG and *n*-butanol molecules were added to the seeds discussed above. Also, two different approaches were followed to determine the importance of conformer selection. In the principal approach, the adsorbates were added to the cluster with the best $\Delta G$ value, step-wise. In the auxiliary approach, two or three molecules of C1 and TGt (as the most stable DEG and *n*-butanol conformers, respectively) were clustered simultaneously on the seeds. The process of DEG and *n*-butanol nucleation on the two seeds and the associated $\Delta G$ values are shown in Figures 4 and S3. Also, the detailed thermodynamics results are reported in Tables 3, 4 and S3. As seen in Figures 4 and S3, A4B3 and DEG give lower $\Delta G$ values throughout the process, and the adsorption free energies remain strongly negative. Therefore, we expect the A4B3/DEG cluster to grow more efficiently than the others, while the T3B2/*n*-butanol cluster likely needs higher vapor concentrations to be detected.

Comparison of Figure 4 with Figure S3 and, also, Tables 3 and 4 with Table S3 demonstrates that while the thermodynamics details are sensitive to the approach used to generate the molecule-seed structures (for example, cumulative $\Delta G$ is obtained as −55.0 and −53.8 kJ $mol^{-1}$ for T3B2/TGt/TGt using the step-wise and simultaneous configurational sampling approaches, respectively), the qualitative results do not depend on the choice of the adsorbate conformer and sampling method. Therefore, in qualitative studies on heterogeneous nucleation of relatively simple organic compounds on ionic seeds, conformational flexibility and step-wise addition of the adsorbates can be neglected. However, quantitative studies are advised to follow the step-wise approach because the most stable conformer does


https://dx.doi.org/10.1021/acs.jpca.0c08373
J. Phys. Chem. A 2020, 124, 10527−10539

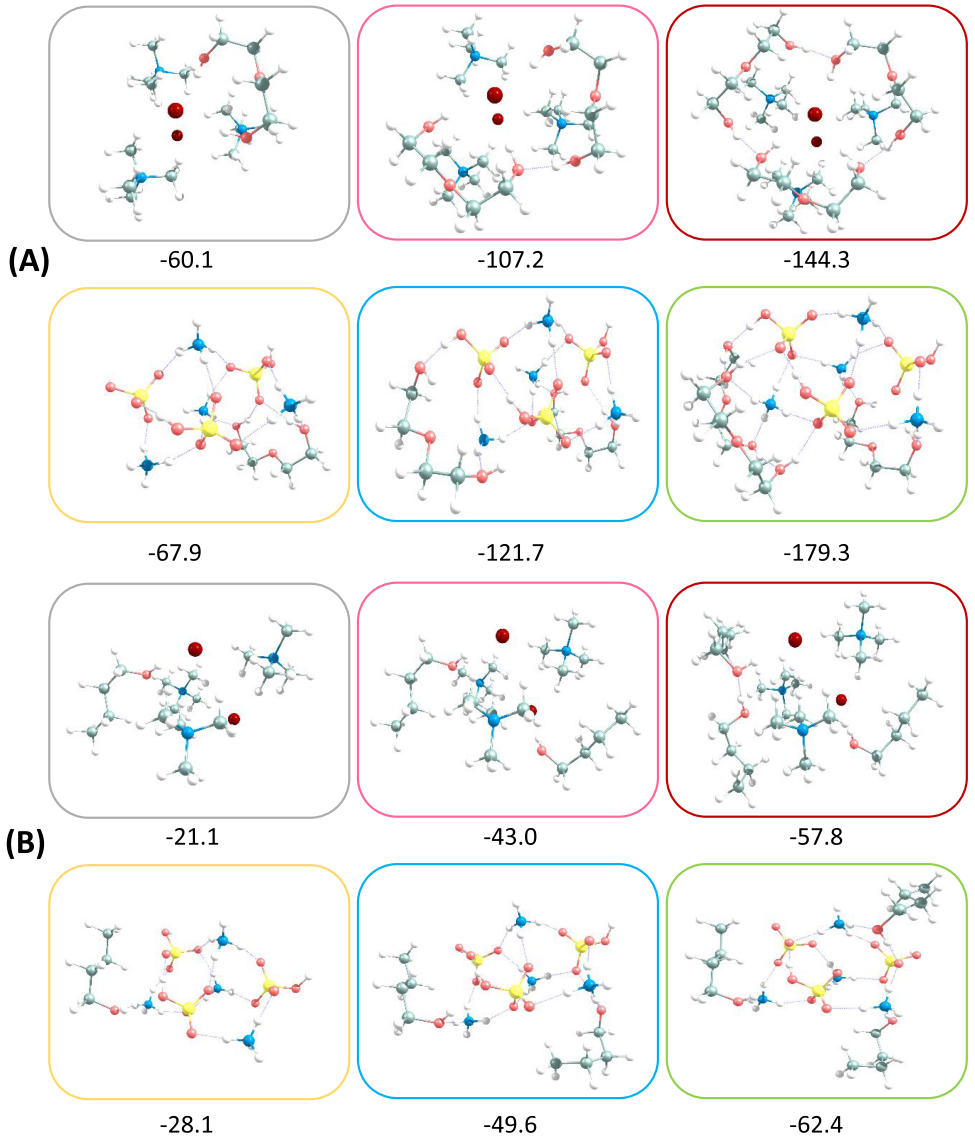


**Figure 4.** Adsorption mode of one to three molecules (left to right) of DEG (A) and *n*-butanol (B) on the $((CH_3)_4N^+)_3(Br^-)_2$ (i.e., T3B2, the upper panels) and $(NH_4^+)_4(HSO_4^-)_3$ (i.e., A4B3, the lower panels) seeds. The values under each panel are the cumulative $\Delta G$ values of DEG or *n*-butanol adsorption at 298.15 K and 1 atm, in kJ mol$^{-1}$. The blue dotted lines represent strong hydrogen bonding.

not necessarily give the true cluster structure. For instance, the nucleation of DEG and *n*-butanol on the A4B3 and T3B2 seeds follows the following path

DEG: A4B3 → A4B3/C1 → A4B3/C1/C5 → A4B3/C1/C5/C1

DEG: T3B2 → T3B2/C5 → T3B2/C5/C5 → T3B2/C5/C5/C9

*n* − butanol: A4B3 → A4B3/TGt → A4B3/TGt/GGt → A4B3/TGt/GGt/TGt

*n* − butanol: T3B2 → T3B2/TGt → T3B2/TGt/TGt → T3B2/TGt/TGt/GGt

As the simultaneous configurational sampling approach is sufficient for qualitative analysis, the effect of temperature on the first steps of the nucleation process was studied by focusing on the C1 and TGt containing clusters, considering the typical operating temperature of CPCs (278−288 K). The results in Figure 5 clearly show that the preference of the A4B3 seed and DEG is not temperature sensitive over the temperature range of 278.15−298.15 K. Also, the reduction of temperature has the same effect on the four cluster sets; it improves C1 and TGt adsorption on the A4B3 and T3B2 seeds mainly by decreasing entropy contribution.

Finally, NBO analysis was performed on the clusters with two or three adsorbate molecules. The results are summarized in Tables S4 and S5. Similar to the one adsorbate−seed NBO results, the main interaction involved in the growth of the clusters is hydrogen bonding. Again, the hydrogen bonding between the A4B3 seed and the DEG adsorbate is stronger than for any of the other combinations. Another important finding highlighted by the NBO results and Figures 4 and S3 is that the DEG or *n*-butanol molecules adsorbed on the seeds can also interact with additional adsorbate molecules. In the case of A4B3, there are many efficient adsorption sites available. Therefore, the DEG and *n*-butanol molecules prefer to attach


https://dx.doi.org/10.1021/acs.jpca.0c08373
J. Phys. Chem. A 2020, 124, 10527−10539

**Table 3. Thermodynamics of Two DEG or *n*-Butanol Adsorption on the $(NH_4^+)_4(HSO_4^-)_3$ (i.e., A4B3) and $((CH_3)_4N^+)_3(Br^-)_2$ (i.e., T3B2) Seeds Using the Most Stable Seed−DEG/*n*-Butanol Clusters (T3B2/C5 and A4B3/C1 for DEG and T3B2/TGt and A4B3/TGt for *n*-Butanol), at the ωB97X-D/def2-TZVP Level[a]**

| | cumulative | | | | | step-wise | | | | |
|---|---|---|---|---|---|---|---|---|---|---|
| adsorbate | Δ*E* | Δ*U* | Δ*H* | Δ*G* | Δ*S* | Δ*E* | Δ*U* | Δ*H* | Δ*G* | Δ*S* |
| | | | | | $((CH_3)_4N^+)_3(Br^-)_2$ | | | | | |
| C1 | −218.2 | −214.1 | −219.0 | −100.5 | −397.7 | −99.5 | −96.9 | −99.4 | −40.3 | −198.1 |
| C3 | −220.0 | −216.8 | −221.8 | −101.2 | −404.4 | −101.3 | −99.6 | −102.1 | −41.1 | −204.8 |
| C5 | −219.5 | −214.6 | −219.5 | −107.2 | −376.6 | −100.8 | −97.4 | −99.9 | −47.1 | −177.0 |
| C9 | −199.6 | −195.5 | −200.5 | −81.1 | −400.4 | −80.9 | −78.3 | −80.8 | −20.9 | −200.8 |
| C10 | −202.0 | −196.7 | −201.7 | −87.8 | −381.8 | −83.3 | −79.5 | −82.0 | −27.7 | −182.2 |
| GG′g | −133.3 | −126.0 | −131.0 | −36.8 | −316.0 | −65.2 | −62.1 | −64.6 | −15.7 | −164.1 |
| GGt | −135.8 | −128.7 | −133.6 | −41.3 | −309.6 | −67.8 | −64.8 | −67.2 | −20.2 | −157.7 |
| GTg′ | −130.4 | −122.9 | −127.8 | −37.6 | −302.5 | −62.4 | −59.0 | −61.4 | −16.6 | −150.5 |
| GGg | −135.8 | −128.7 | −133.6 | −41.6 | −308.6 | −67.8 | −64.8 | −67.2 | −20.6 | −156.6 |
| TGt | −140.5 | −133.3 | −138.3 | −43.0 | −319.6 | −72.4 | −69.4 | −71.9 | −21.9 | −167.6 |
| | | | | | $(NH_4^+)_4(HSO_4^-)_3$ | | | | | |
| C1 | −232.2 | −228.6 | −233.6 | −121.2 | −376.9 | −112.2 | −110.1 | −112.6 | −53.3 | −199.0 |
| C3 | −230.7 | −228.6 | −233.6 | −116.5 | −392.9 | −110.7 | −110.2 | −112.7 | −48.6 | −215.0 |
| C5 | −234.2 | −232.5 | −237.5 | −121.7 | −388.4 | −114.3 | −114.1 | −116.5 | −53.8 | −210.5 |
| C9 | −216.7 | −213.0 | −218.0 | −111.6 | −356.9 | −96.7 | −94.5 | −97.0 | −43.7 | −179.0 |
| C10 | −226.6 | −223.4 | −228.4 | −114.5 | −382.0 | −106.6 | −105.0 | −107.5 | −46.6 | −204.0 |
| GG′g | −140.0 | −134.3 | −139.3 | −45.1 | −315.8 | −64.3 | −61.5 | −64.0 | −17.0 | −157.5 |
| GGt | −142.9 | −137.3 | −142.2 | −49.6 | −310.8 | −67.2 | −64.5 | −66.9 | −21.5 | −152.5 |
| GTg′ | −141.6 | −136.4 | −141.4 | −41.7 | −334.4 | −65.9 | −63.6 | −66.1 | −13.6 | −176.2 |
| GGg | −140.5 | −134.9 | −139.9 | −45.9 | −315.2 | −64.8 | −62.1 | −64.6 | −17.8 | −156.9 |
| TGt | −147.2 | −142.0 | −146.9 | −47.4 | −333.9 | −71.5 | −69.2 | −71.6 | −19.3 | −175.7 |

[a]Δ*E*, Δ*U*, Δ*H*, and Δ*G* are in kJ mol$^{-1}$, while Δ*S* is in J mol$^{-1}$. All data refer to 298.15 K and 1 atm.

**Table 4. Thermodynamics of Three DEG or *n*-Butanol Adsorption on the $(NH_4^+)_4(HSO_4^-)_3$ (i.e., A4B3) and $((CH_3)_4N^+)_3(Br^-)_2$ (i.e., T3B2) Seeds using the Most Stable Seed−DEG/*n*-Butanol Clusters (T3B2/C5/C5 and A4B3/C1/C5 for DEG and T3B2/TGt/TGt and A4B3/TGt/GGt for *n*-Butanol), at the ωB97X-D/def2-TZVP Level[a]**

| | cumulative | | | | | step-wise | | | | |
|---|---|---|---|---|---|---|---|---|---|---|
| adsorbate | Δ*E* | Δ*U* | Δ*H* | Δ*G* | Δ*S* | Δ*E* | Δ*U* | Δ*H* | Δ*G* | Δ*S* |
| | | | | | $((CH_3)_4N^+)_3(Br^-)_2$ | | | | | |
| C1 | −320.2 | −314.8 | −322.2 | −141.9 | −604.8 | −100.7 | −100.2 | −102.7 | −34.6 | −228.2 |
| C3 | −316.8 | −312.3 | −319.7 | −136.1 | −615.7 | −97.3 | −97.7 | −100.2 | −28.9 | −239.1 |
| C5 | −319.4 | −313.8 | −321.2 | −140.8 | −605.1 | −99.9 | −99.2 | −101.7 | −33.6 | −228.4 |
| C9 | −326.4 | −322.1 | −329.6 | −144.3 | −621.4 | −106.9 | −107.5 | −110.0 | −37.0 | −244.8 |
| C10 | −303.2 | −297.6 | −305.0 | −124.2 | −606.7 | −83.7 | −83.0 | −85.5 | −16.9 | −230.0 |
| GG′g | −205.8 | −196.3 | −203.7 | −50.4 | −514.2 | −65.3 | −63.0 | −65.5 | −7.4 | −194.6 |
| GGt | −211.0 | −202.6 | −210.1 | −57.8 | −510.7 | −70.5 | −69.3 | −71.8 | −14.8 | −191.1 |
| GTg′ | −197.2 | −186.4 | −193.8 | −51.2 | −478.2 | −56.8 | −53.0 | −55.5 | −8.2 | −158.6 |
| GGg | −210.9 | −202.4 | −209.8 | −56.6 | −514.0 | −70.5 | −69.0 | −71.5 | −13.6 | −194.4 |
| TGt | −199.9 | −188.7 | −196.1 | −55.0 | −473.4 | −59.4 | −55.4 | −57.8 | −12.0 | −153.8 |
| | | | | | $(NH_4^+)_4(HSO_4^-)_3$ | | | | | |
| C1 | −359.4 | −358.0 | −365.4 | −179.3 | −624.4 | −125.1 | −125.5 | −127.9 | −57.6 | −236.0 |
| C3 | −339.3 | −337.1 | −344.5 | −163.6 | −606.9 | −105.1 | −104.6 | −107.0 | −41.9 | −218.4 |
| C5 | −338.2 | −335.0 | −342.5 | −162.7 | −602.9 | −104.0 | −102.5 | −105.0 | −41.1 | −214.5 |
| C9 | −330.3 | −325.6 | −333.0 | −160.8 | −577.8 | −96.1 | −93.1 | −95.5 | −39.1 | −189.3 |
| C10 | −344.0 | −342.2 | −349.6 | −168.7 | −606.7 | −109.7 | −109.7 | −112.2 | −47.1 | −218.3 |
| GG′g | −197.7 | −188.7 | −196.2 | −58.2 | −197.7 | −54.8 | −51.5 | −53.9 | −8.7 | −151.8 |
| GGt | −200.1 | −190.4 | −197.9 | −60.1 | −200.1 | −57.2 | −53.2 | −55.6 | −10.6 | −151.2 |
| GTg′ | −203.1 | −193.9 | −201.4 | −60.3 | −203.1 | −60.1 | −56.6 | −59.1 | −10.7 | −162.3 |
| GGg | −204.9 | −195.7 | −203.1 | −60.3 | −204.9 | −61.9 | −58.4 | −60.8 | −10.7 | −168.0 |
| TGt | −205.3 | −196.6 | −204.0 | −62.4 | −205.3 | −62.4 | −59.3 | −61.8 | −12.9 | −164.0 |

[a]Δ*E*, Δ*U*, Δ*H*, and Δ*G* are in kJ mol$^{-1}$, while Δ*S* is in J mol$^{-1}$. All data refer to 298.15 K and 1 atm.

to various parts of the A4B3 seeds. However, T3B2 does not provide many efficient adsorption sites. Consequently, the adsorbed DEG and *n*-butanol molecules, which have the potential of hydrogen bonding, assist the adsorption/nucleation process through hydrogen bonding to the adsorbing DEG and *n*-butanol conformers. In other words, when the seeds themselves



https://dx.doi.org/10.1021/acs.jpca.0c08373
J. Phys. Chem. A 2020, 124, 10527−10539

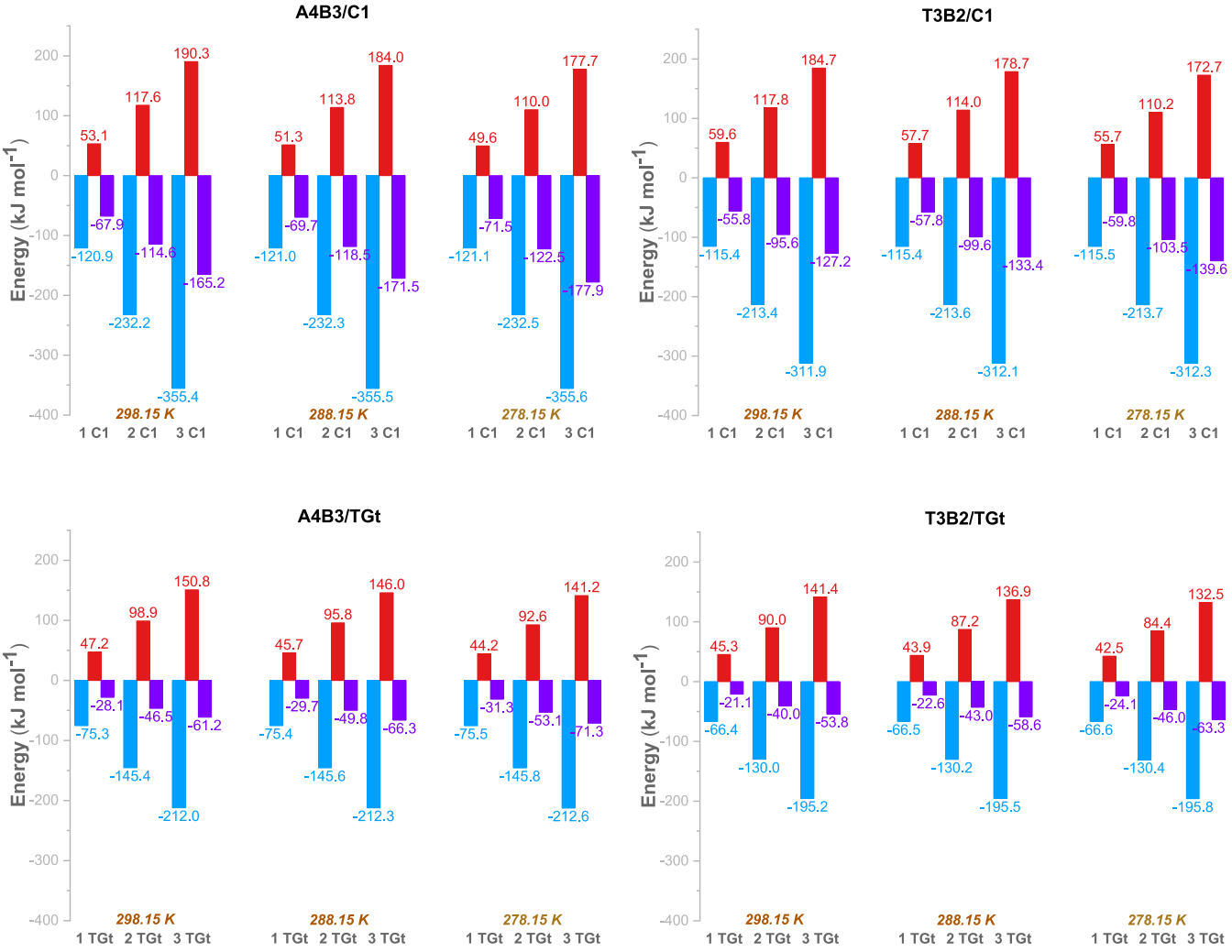


**Figure 5.** Temperature effect on thermodynamics of one to three DEG (conformer C1) or *n*-butanol (conformer TGt) simultaneous adsorption on the $(NH_4^+)_4(HSO_4^-)_3$ (i.e., A4B3) and $((CH_3)_4N^+)_3(Br^-)_2$ (i.e., T3B2) seeds, at the $\omega$B97X-D/def2-TZVP Level. The blue, red, and violet bars, respectively, display $\Delta H$, $-T\Delta S$, and $\Delta G$ in kJ mol$^{-1}$, at 1 atm.

do not have available adsorption sites for further adsorbates, the process of cluster growth can continue through adsorbate–adsorbate interactions. Also, we note that hydrogen-bonding capability should not be judged solely based on the number of hydrogen-bonding acceptor and donor groups of the organic compound because the configuration of the adsorbates around the seeds is an important factor. For example, Figure 4 shows that DEG can extend around the seeds while *n*-butanol might prefer adsorbing from its hydroxyl head and extending its alkyl chain outwards. As the alkyl chain is a weaker hydrogen-bonding acceptor relative to the hydroxyl moiety, the nucleation of *n*-butanol can be gradually hindered by the adsorbate layer covering the seed. Therefore, DEG is expected to be more efficient in adsorbing the next round of adsorbate molecules from the gas phase.

## 4. CONCLUSIONS

We investigated the heterogeneous nucleation of DEG and *n*-butanol on $(NH_4^+)_4(HSO_4^-)_3$ and $((CH_3)_4N^+)_3(Br^-)_2$ seeds by studying the intermolecular vapor–vapor and seed–vapor interactions. While this work can be extended by considering the dynamical aspects of the process (for example, using molecular dynamics simulation analogous to the studies of Chowdhary et al.,[61] Suh and Yasuoka,[62] Radola et al.,[63] and Karadima et al.[64]), the details of the chemical interactions governing the process can only be extracted from quantum chemical modeling. Based on our results, we conclude:

1. Different vapors and vapor conformers do not nucleate on different seeds similarly. For *n*-butanol, the TGt and GGt conformers are preferably adsorbed during the starting steps of heterogeneous nucleation, while the C1 and C5 conformers are preferred in the case of DEG.
2. The key factor determining the progress of the nucleation process is the extent of hydrogen bonding. Therefore, the number of hydrogen bond donors and acceptors controls the extent of nucleation in seed/vapor systems.
3. When the seed does not offer many potential hydrogen-bonding sites (like the $((CH_3)_4N^+)_3(Br^-)_2$ seed), hydrogen bonding between the adsorbed vapor molecules can help stabilizing the cluster.
4. Simulation of the adsorption of the first vapor molecules on seeds likely predicts the qualitative preferences in heterogeneous nucleation.
5. Both step-wise and simultaneous adsorbate addition approaches give the same qualitative results with insignificant differences in the adsorption thermodynam-


https://dx.doi.org/10.1021/acs.jpca.0c08373
J. Phys. Chem. A 2020, 124, 10527–10539

ics. Therefore, studies on heterogeneous nucleation can follow either of the approaches, at least for qualitative results.

6. In general, the nucleation probability in the four studied seed/vapor systems follows the order DEG/$(NH_4^+)_4(HSO_4^-)_3$ > DEG/$((CH_3)_4N^+)_3(Br^-)_2$ > *n*-butanol/$(NH_4^+)_4(HSO_4^-)_3$ > *n*-butanol/$((CH_3)_4N^+)_3(Br^-)_2$. This order does not change with temperature over the temperature range of 278.15−298.15 K.

7. Agreement of the modeling results with experimental observations suggests that our CPC modeling approach is applicable to heterogeneous nucleation on hydrocarbon seeds.

As the efficiency of nanoparticle detection by CPCs depends on nucleation probability, together with the facts that the higher nucleation rate is expected when the vapor molecules are adsorbed more strongly and that the driving interaction is hydrogen bonding, the results suggest that CPCs should adopt a working fluid that has the highest potential of hydrogen bond formation. The higher potential can be interpreted as the presence of more hydroxyl, ether oxygen, carboxylic, and nitrogen-containing functional groups, as well as any other hydrogen bond acceptor/donor groups. Importantly, a higher potential of hydrogen bonding during heterogeneous nucleation also means a higher potential of homogeneous nucleation of the vapor molecules. Though heterogeneous nucleation dominates homogeneous clustering of the condensing fluid in CPCs, the vapor saturation conditions should be adjusted to minimize the detection error caused by homogeneous nucleation of the working vapor. Furthermore, in the choice of the working fluid, the vapors with long alkyl chains are expected to nucleate less efficiently because the long chains tend to head outwards from seeds and their lower potency of strong interaction hinders further growth of the adsorbate shell on the seeds. On the other hand, the conformational flexibility of the vapor can help in creating the most stable seeds/vapor complexes and improve the nucleation process.

As a result, detection is most effective when the seed has many hydrogen-bonding sites exposed to the vapor molecules and the seed's constituents are capable of establishing strong hydrogen-bonding networks. Also, the ionic nature of seeds can promote the extent of hydrogen bonding and nucleation. On the other hand, activation of the seeds with a hydrocarbon nature, many alkyl groups, and few hydrogen-bonding sites is expected to be more challenging. Finally, configurational flexibility of seeds (i.e., the rearrangement possibility of the seed components) can increase the effectiveness of the interactions and nucleation by providing an opportunity for the vapor molecules to interact with less spatial restriction.

## ■ ASSOCIATED CONTENT

### Supporting Information

The Supporting Information is available free of charge at https://pubs.acs.org/doi/10.1021/acs.jpca.0c08373.

Results of computational level validation (Figures S1 and S2, and Table S1), and structures, thermodynamics results and NBO analysis of two/three C1, TGt and GTg′ molecules added simultaneously to the seeds (Figure S3 and Tables S2−S5) (PDF)

The frequency calculation output files of all vapor conformers and the most stable structures of all seeds and seed−DEG/n-butanol clusters (ZIP)

## ■ AUTHOR INFORMATION


### Corresponding Author

**Fatemeh Keshavarz** − *Institute for Atmospheric and Earth System Research/Physics, Faculty of Science, University of Helsinki, 00014 Helsinki, Finland;* orcid.org/0000-0003-2189-7809; Email: fatemeh.keshavarz@helsinki.fi

### Authors

**Theo Kurtén** − *Department of Chemistry, Faculty of Science, University of Helsinki, FI-00014 Helsinki, Finland;* orcid.org/0000-0002-6416-4931

**Hanna Vehkamäki** − *Institute for Atmospheric and Earth System Research/Physics, Faculty of Science, University of Helsinki, 00014 Helsinki, Finland;* orcid.org/0000-0002-5018-1255

**Juha Kangasluoma** − *Institute for Atmospheric and Earth System Research/Physics, Faculty of Science, University of Helsinki, 00014 Helsinki, Finland; Aerosol and Haze Laboratory, Beijing Advanced Innovation Center for Soft Matter Science and Engineering, Beijing University of Chemical Technology, 100029 Beijing, China;* orcid.org/0000-0002-1639-1187

Complete contact information is available at: https://pubs.acs.org/10.1021/acs.jpca.0c08373


### Notes

The authors declare no competing financial interest.

## ■ ACKNOWLEDGMENTS

This study is financially supported by the ERC Project 692891-DAMOCLES, UHEL 3-year grant 75284132, University of Helsinki, Faculty of Science ATMATH project, and Academy of Finland project 1325656. The computational resources provided by the CSC-IT Center for Science in Espoo, Finland, are greatly acknowledged.

## ■ REFERENCES


(1) Kulmala, M.; Vehkamäki, H.; Petäjä, T.; Dal Maso, M.; Lauri, A.; Kerminen, V.-M.; Birmili, W.; McMurry, P. H. Formation and growth rates of ultrafine atmospheric particles: a review of observations. *J. Aerosol Sci.* **2004**, *35*, 143−176.

(2) Rönkkö, T.; Timonen, H. Overview of sources and characteristics of nanoparticles in urban traffic-influenced areas. *J. Alzheimer's Dis.* **2019**, *72*, 15−28.

(3) Viitanen, A.-K.; Uuksulainen, S.; Koivisto, A. J.; Hämeri, K.; Kauppinen, T. Workplace measurements of ultrafine particles—a literature review. *Ann. Work Exposures Health* **2017**, *61*, 749−758.

(4) Guo, S.; Hu, M.; Zamora, M. L.; Peng, J.; Shang, D.; Zheng, J.; Du, Z.; Wu, Z.; Shao, M.; Zeng, L.; et al. Elucidating severe urban haze formation in China. *Proc. Natl. Acad. Sci. U.S.A.* **2014**, *111*, 17373−17378.

(5) Kerminen, V.-M.; Paramonov, M.; Anttila, T.; Riipinen, I.; Fountoukis, C.; Korhonen, H.; Asmi, E.; Laakso, L.; Lihavainen, H.; Swietlicki, E.; et al. Cloud condensation nuclei production associated with atmospheric nucleation: a synthesis based on existing literature and new results. *Atmos. Chem. Phys.* **2012**, *12*, 12037−12059.

(6) Fan, J.; Rosenfeld, D.; Zhang, Y.; Giangrande, S. E.; Li, Z.; Machado, L. A. T.; Martin, S. T.; Yang, Y.; Wang, J.; Artaxo, P.; et al. Substantial convection and precipitation enhancements by ultrafine aerosol particles. *Science* **2018**, *359*, 411−418.

(7) Kwon, H.-S.; Ryu, M. H.; Carlsten, C. Ultrafine particles: unique physicochemical properties relevant to health and disease. *Exp. Mol. Med.* **2020**, *52*, 318−328.
(8) Spracklen, D. V.; Carslaw, K. S.; Kulmala, M.; Kerminen, V.-M.; Sihto, S.-L.; Riipinen, I.; Merikanto, J.; Mann, G. W.; Chipperfield, M. P.; Wiedensohler, A.; et al. Contribution of particle formation to global cloud condensation nuclei concentrations. *Geophys. Res. Lett.* **2008**, *35*, L06808−L06812.
(9) Kangasluoma, J.; Cai, R.; Jiang, J.; Deng, C.; Stolzenburg, D.; Ahonen, L. R.; Chan, T.; Fu, Y.; Kim, C.; Laurila, T. M.; et al. Overview of measurements and current instrumentation for 1−10 nm aerosol particle number size distributions. *J. Aerosol Sci.* **2020**, *148*, 105584−105612.
(10) Kangasluoma, J.; Attoui, M. Review of sub-3 nm condensation particle counters, calibrations, and cluster generation methods. *Aerosol Sci. Technol.* **2019**, *53*, 1277−1310.
(11) McMurry, P. H. The history of condensation nucleus counters. *Aerosol Sci. Technol.* **2000**, *33*, 297−322.
(12) Hering, S. V.; Stolzenburg, M. R.; Quant, F. R.; Oberreit, D. R.; Keady, P. B. A laminar-flow, water-based condensation particle counter (WCPC). *Aerosol Sci. Technol.* **2005**, *39*, 659−672.
(13) Iida, K.; Stolzenburg, M. R.; McMurry, P. H. Effect of working fluid on sub-2 nm particle detection with a laminar flow ultrafine condensation particle counter. *Aerosol Sci. Technol.* **2009**, *43*, 81−96.
(14) Kangasluoma, J.; Kuang, C.; Wimmer, D.; Rissanen, M. P.; Lehtipalo, K.; Ehn, M.; Worsnop, D. R.; Wang, J.; Kulmala, M.; Petäjä, T. Sub-3 nm particle size and composition dependent response of a nano-CPC battery. *Atmos. Meas. Tech.* **2014**, *7*, 689−700.
(15) Kuang, C.; Chen, M.; McMurry, P. H.; Wang, J. Modification of laminar flow ultrafine condensation particle counters for the enhanced detection of 1 nm condensation nuclei. *Aerosol Sci. Tech.* **2012**, *46*, 309−315.
(16) Wlasits, P. J.; Stolzenburg, D.; Tauber, C.; Brilke, S.; Schmitt, S. H.; Winkler, P. M.; Wimmer, D. Counting on chemistry: laboratory evaluation of seed-material-dependent detection efficiencies of ultrafine condensation particle counters. *Atmos. Meas. Tech.* **2020**, *13*, 3787−3798.
(17) Jiang, J.; Chen, M.; Kuang, C.; Attoui, M.; McMurry, P. H. Electrical mobility spectrometer using a diethylene glycol condensation particle counter for measurement of aerosol size distributions down to 1 nm. *Aerosol Sci. Technol.* **2011**, *45*, 510−521.
(18) Ehn, M.; Thornton, J. A.; Kleist, E.; Sipilä, M.; Junninen, H.; Pullinen, I.; Springer, M.; Rubach, F.; Tillmann, R.; Lee, B.; et al. A large source of low-volatility secondary organic aerosol. *Nature* **2014**, *506*, 476−479.
(19) Kangasluoma, J.; Samodurov, A.; Attoui, M.; Franchin, A.; Junninen, H.; Korhonen, F.; Kurtén, T.; Vehkamäki, H.; Sipilä, M.; Lehtipalo, K.; et al. Heterogeneous nucleation onto ions and neutralized ions: Insights into sign-preference. *J. Phys. Chem. C* **2016**, *120*, 7444−7450.
(20) Wimmer, D.; Lehtipalo, K.; Franchin, A.; Kangasluoma, J.; Kreissl, F.; Kürten, A.; Kupc, A.; Metzger, A.; Mikkilä, J.; Petäjä, T.; et al. Performance of diethylene glycol-based particle counters in the sub-3 nm size range. *Atmos. Meas. Tech.* **2013**, *6*, 1793−1804.
(21) Vanhanen, J.; Mikkilä, J.; Lehtipalo, K.; Sipilä, M.; Manninen, H. E.; Siivola, E.; Petäjä, T.; Kulmala, M. Particle size magnifier for nano-CN detection. *Aerosol Sci. Technol.* **2011**, *45*, 533−542.
(22) Oh, K. J.; Gao, G. T.; Zeng, X. C. Nucleation of water and methanol droplets on cations and anions: the sign preference. *Phys. Rev. Lett.* **2001**, *86*, 5080−5083.
(23) Nadykto, A. B.; Yu, F.; Herb, J. Towards understanding the sign preference in binary atmospheric nucleation. *Phys. Chem. Chem. Phys.* **2008**, *10*, 7073−7078.
(24) Kurtén, T.; Ortega, I. K.; Vehkamäki, H. The sign preference in sulfuric acid nucleation. *J. Mol. Struct.: THEOCHEM* **2009**, *901*, 169−173.
(25) Zhang, H.; Kupiainen-Määttä, O.; Zhang, X.; Molinero, V.; Zhang, Y.; Li, Z. The enhancement mechanism of glycolic acid on the formation of atmospheric sulfuric acid−ammonia molecular clusters. *J. Chem. Phys.* **2017**, *146*, 184308−184311.
(26) Wang, C.-Y.; Jiang, S.; Wang, Z.-Q.; Liu, Y.-R.; Wen, H.; Huang, T.; Han, Y.-J.; Huang, W. Can formaldehyde contribute to atmospheric new particle formation from sulfuric acid and water? *Atmos. Environ.* **2019**, *201*, 323−333.
(27) Kurtén, T.; Sundberg, M. R.; Vehkamäki, H.; Noppel, M.; Blomqvist, J.; Kulmala, M. Ab initio and density functional theory reinvestigation of gas-phase sulfuric acid monohydrate and ammonium hydrogen sulfate. *J. Phys. Chem. A* **2006**, *110*, 7178−7188.
(28) Leverentz, H. R.; Siepmann, J. I.; Truhlar, D. G.; Loukonen, V.; Vehkamaki, H. Energetics of atmospherically implicated clusters made of sulfuric acid, ammonia, and dimethyl amine. *J. Phys. Chem. A* **2013**, *117*, 3819−3825.
(29) Tsona, N. T.; Henschel, H.; Bork, N.; Loukonen, V.; Vehkamäki, H. Structures, hydration, and electrical mobilities of bisulfate ion−sulfuric acid−ammonia/dimethylamine clusters: a computational study. *J. Phys. Chem. A* **2015**, *119*, 9670−9679.
(30) Yang, Y.; Johnson, C. J. Hydration motifs of ammonium bisulfate clusters of relevance to atmospheric new particle formation. *Faraday Discuss.* **2019**, *217*, 47−66.
(31) Dib, E.; Alonso, B.; Mineva, T. DFT-D study of 14N nuclear quadrupolar interactions in tetra-n-alkyl ammonium halide crystals. *J. Phys. Chem. A* **2014**, *118*, 3525−3533.
(32) Sawicka, M.; Storoniak, P.; Skurski, P.; Błażejowski, J.; Rak, J. TG-FTIR, DSC and quantum chemical studies of the thermal decomposition of quaternary methylammonium halides. *Chem. Phys.* **2006**, *324*, 425−437.
(33) Johnson, C. J.; Johnson, M. A. Vibrational spectra and fragmentation pathways of size-selected, D2-tagged ammonium/methylammonium bisulfate clusters. *J. Phys. Chem. A* **2013**, *117*, 13265−13274.
(34) DePalma, J. W.; Doren, D. J.; Johnston, M. V. Formation and growth of molecular clusters containing sulfuric acid, water, ammonia, and dimethylamine. *J. Phys. Chem. A* **2014**, *118*, 5464−5473.
(35) Li, L.; Kumar, M.; Zhu, C.; Zhong, J.; Francisco, J. S.; Zeng, X. C. Near-barrierless ammonium bisulfate formation via a loop-structure promoted proton-transfer mechanism on the surface of water. *J. Am. Chem. Soc.* **2016**, *138*, 1816−1819.
(36) Mondal, A.; Balasubramanian, S. Vibrational signatures of cation−anion hydrogen bonding in ionic liquids: a periodic density functional theory and molecular dynamics study. *J. Phys. Chem. B* **2015**, *119*, 1994−2002.
(37) Mann, L.; Voßnacker, P.; Müller, C.; Riedel, S. $[NMe_4][I_4Br_5]$: a new iodobromide from an ionic liquid with halogen−halogen interactions. *Chem. - Eur. J.* **2017**, *23*, 244−249.
(38) Nadykto, A.; Yu, F.; Jakovleva, M.; Herb, J.; Xu, Y. Amines in the Earth's atmosphere: a density functional theory study of the thermochemistry of pre-nucleation clusters. *Entropy* **2011**, *13*, 554−569.
(39) Yang, Y.; Waller, S. E.; Kreinbihl, J. J.; Johnson, C. J. Direct link between structure and hydration in ammonium and aminium bisulfate clusters implicated in atmospheric new particle formation. *J. Phys. Chem. Lett.* **2018**, *9*, 5647−5652.
(40) Myllys, N.; Chee, S.; Olenius, T.; Lawler, M.; Smith, J. Molecular-level understanding of synergistic effects in sulfuric acid−amine−ammonia mixed clusters. *J. Phys. Chem. A* **2019**, *123*, 2420−2425.
(41) Weigend, F.; Ahlrichs, R. Balanced basis sets of split valence, triple zeta valence and quadruple zeta valence quality for H to Rn: design and assessment of accuracy. *Phys. Chem. Chem. Phys.* **2005**, *7*, 3297−3305.
(42) Weigend, F. Accurate Coulomb-fitting basis sets for H to Rn. *Phys. Chem. Chem. Phys.* **2006**, *8*, 1057−1065.
(43) Voss, J. M.; Marsh, B. M.; Zhou, J.; Garand, E. Interaction between ionic liquid cation and water: infrared predissociation study of $[bmim]^+ \cdot (H_2O)_n$ clusters. *Phys. Chem. Chem. Phys.* **2016**, *18*, 18905−18913.
(44) Frisch, M. J.; Trucks, G. W.; Schlegel, H. B.; Scuseria, G. E.; Robb, M. A.; Cheeseman, J. R.; Scalmani, G.; Barone, V.; Petersson, G.


https://dx.doi.org/10.1021/acs.jpca.0c08373
J. Phys. Chem. A 2020, 124, 10527−10539

A.; Nakatsuji, H.; et al. *Gaussian 16*, revision A.03; Gaussian Inc.: Wallingford, CT, 2016.
(45) Neese, F. The ORCA program system. *Wiley Interdiscip. Rev.: Comput. Mol. Sci.* **2012**, *2*, 73−78.
(46) Lee, K. L. K.; McCarthy, M. Bayesian analysis of theoretical rotational constants from low-cost electronic structure methods. *J. Phys. Chem. A* **2020**, *124*, 898−910.
(47) DiLabio, G. A.; Otero-de-la-Roza, A. Noncovalent interactions in density functional theory. *Rev. Comput. Chem.* **2016**, *29*, 1−97.
(48) Almeida, J.; Schobesberger, S.; Kürten, A.; Ortega, I. K.; Kupiainen-Määttä, O.; Praplan, A. P.; Adamov, A.; Amorim, A.; Bianchi, F.; Breitenlechner, M.; et al. Molecular understanding of sulphuric acid−amine particle nucleation in the atmosphere. *Nature* **2013**, *502*, 359−363.
(49) Kubečka, J.; Besel, V.; Kurtén, T.; Myllys, N.; Vehkamäki, H. Configurational sampling of noncovalent (atmospheric) molecular clusters: sulfuric acid and guanidine. *J. Phys. Chem. A* **2019**, *123*, 6022−6033.
(50) Zhang, J.; Dolg, M. ABCluster: the artificial bee colony algorithm for cluster global optimization. *Phys. Chem. Chem. Phys.* **2015**, *17*, 24173−24181.
(51) Zhang, J.; Dolg, M. Global optimization of clusters of rigid molecules using the artificial bee colony algorithm. *Phys. Chem. Chem. Phys.* **2016**, *18*, 3003−3010.
(52) Olsen, R.; Kvamme, B.; Kuznetsova, T. Free energy of solvation and Henry's law solubility constants for mono-, di-and tri-ethylene glycol in water and methane. *Fluid Phase Equilib.* **2016**, *418*, 152−159.
(53) Cerar, J.; Lajovic, A.; Jamnik, A.; Tomšič, M. Performance of various models in structural characterization of n-butanol: molecular dynamics and X-ray scattering studies. *J. Mol. Liq.* **2017**, *229*, 346−357.
(54) Mayo, S. L.; Olafson, B. D.; Goddard, W. A. DREIDING: a generic force field for molecular simulations. *J. Phys. Chem. A* **1990**, *94*, 8897−8909.
(55) Lamonte, K.; Gómez Gualdrón, D. A.; Cabrales-Navarro, F. A.; Scanlon, L. G.; Sandi, G.; Feld, W.; Balbuena, P. B. Molecular dynamics simulations of $H_2$ adsorption in tetramethyl ammonium lithium phthalocyanine crystalline structures. *J. Phys. Chem. B* **2008**, *112*, 15775−15782.
(56) Bannwarth, C.; Ehlert, S.; Grimme, S. GFN2-xTB—An accurate and broadly parametrized self-consistent tight-binding quantum chemical method with multipole electrostatics and density-dependent dispersion contributions. *J. Chem. Theory Comput.* **2019**, *15*, 1652−1671.
(57) Grimme, S.; Bannwarth, C.; Shushkov, P. A robust and accurate tight-binding quantum chemical method for structures, vibrational frequencies, and noncovalent interactions of large molecular systems parametrized for all spd-block elements (Z = 1−86). *J. Chem. Theory Comput.* **2017**, *13*, 1989−2009.
(58) Black, G.; Simmie, J. M. Barrier heights for H-atom abstraction by $H\dot{O}_2$ from n-butanol—A simple yet exacting test for model chemistries? *J. Comput. Chem.* **2010**, *31*, 1236−1248.
(59) Moc, J.; Simmie, J. M.; Curran, H. J. The elimination of water from a conformationally complex alcohol: A computational study of the gas phase dehydration of n-butanol. *J. Mol. Struct.* **2009**, *928*, 149−157.
(60) Acree, W. E., Jr.; Chickos, J. S. *Phase Transition Enthalpy Measurements of Organic and Organometallic Compounds, NIST Chemistry WebBook, NIST Standard Reference Database Number 69*, National Institute of Standards and Technology: Gaithersburg, MD, 2016. https://webbook.nist.gov/chemistry/ (accessed Sept 9, 2020).
(61) Chowdhary, J.; Ladanyi, B. M. Molecular dynamics simulation of aerosol-OT reverse micelles. *J. Phys. Chem. B* **2009**, *113*, 15029−15039.
(62) Suh, D.; Yasuoka, K. Nanoparticle growth analysis by molecular dynamics: spherical seed. *J. Phys. Chem. B* **2011**, *115*, 10631−10645.
(63) Radola, B.; Picaud, S.; Vardanega, D.; Jedlovszky, P. Analysis of mixed formic and acetic acid aggregates interacting with water: a molecular dynamics simulation study. *J. Phys. Chem. C* **2017**, *121*, 13863−13875.
(64) Karadima, K. S.; Mavrantzas, V. G.; Pandis, S. N. Molecular dynamics simulation of the local concentration and structure in multicomponent aerosol nanoparticles under atmospheric conditions. *Phys. Chem. Chem. Phys.* **2017**, *19*, 16681−16692.


https://dx.doi.org/10.1021/acs.jpca.0c08373
*J. Phys. Chem. A* 2020, 124, 10527−10539